Supporting Information

1. Materials and Methods

Materials.
NH_4NCS (97.5%) and CsBr (99.9%) were purchased from Alfa Aesar and Mo (purity 99.95, 100 mesh) from Strem Chemicals. THF (GPR Rectapur, purity>99%,) was purchased from VWR. All aqueous solutions were prepared with MilliQ water (18.2 $M\Omega.cm^{-1}$) purified using a Purelab Prima system.

Synthesis of octahedral molybdenum cluster precursors.
$Cs_2[Mo_6Br^i_8Br^a_6]$ was prepared according to experimental protocols reported in the literature.[1] $(NH_4)_2[Mo_6Br^i_8(NCS)^a_6]$ was prepared from $Cs_2[Mo_6Br^i_8Br^a_6]$ by interaction with NH_4NCS in a water : ethanol mixture (50:50). 1 g of $Cs_2[Mo_6Br^i_8Br^a_6]$ and 1g of NH_4NCS were dissolved in 50 ml of a 1:1 mixture of water and ethanol using magnetic stirring. After full dissolution, the temperature was increased to 80°C until precipitation of $(NH_4)_2[Mo_6Br^i_8(NCS)^a_6]$. After elimination of the solvent, the precipitate was dissolved in acetone and the solution was filtrated. A yellow powder was obtained after evaporation of acetone (yield: 97%). Additional analysis by using X-ray powder diffraction, EDS, FTIR and Raman spectroscopies of $Cs_2[Mo_6Br^i_8Br^a_6]$ and $(NH_4)_2[Mo_6Br^i_8(NCS)^a_6]$ did not evidence the presence of any impurities.

Self-Assembly of nanospheres and nanocapsules.
A solution of octahedral cluster precursor (1mmol.L^{-1}) was prepared in THF. Then 200 µL of this solution was poured in a vial, 800 µL of water was added and the mixture vigorously vortexed. The suspension was left to rest for 24 hours before heating to 40°C for 15 hours. It was then centrifuged and the pellet suspended in 1 mL of water.

Raman spectrometry.
Raman spectra were recorded using a LabRam HR800 Raman micro-Raman spectrometer (Horiba Scientific). To avoid fluorescence background and to preserve the sample, we used an excitation wavelength of 785 nm from a XTRA (TOPTICA) laser diode. Measurements have been performed in back scattering configuration with a 100x objective. Power laser was adjusted to avoid sample heating.

Luminescence.
The luminescence spectra were recorded on a Spectrolog 3 (Horiba Jobin Yvon) fluorimeter. The production of O_2 ($^1\Delta g$), via photosensitization from the cluster species was observed by the direct measurement of the characteristic emission at 1270 nm of O_2 ($^1\Delta g$) singlet oxygen emission, recorded using a PM Hamamatsu PMTH10330-75 operating in the spectral window (950 nm -1700 nm) by exciting samples in the solid state using a 375 nm laser diode (delta diode, Horiba Jobin Yvon).

Electron Microscopy.
Transmission electron microscopy was performed using a JEOL JEM-1400 operating at 120 kV and equipped with a GATAN Orius 1000 camera. High resolution TEM micrographs, HAADF-STEM and Energy Dispersive X-ray Spectroscopy analysis (STEM-EDS), were performed on a JEOL JEM-2100F at 200 kV. Scanning electron microscopy was performed using a JEOL 7100f "through-the-lens system" (TTLS) at 10 kV voltage, equipped with a tungsten tip and a Everhart-Thornley detector.

Light Scattering.
Dynamic Light scattering (DLS) monitoring was performed with a Nanosizer (Malvern Instruments). DLS measures the hydrodynamic diameter (D_h) of nano-objects through the analysis of the fluctuations of the scattered intensity. It corresponds to

the size of the diffusing object, including its cohort of associated ions within the limits of the electrostatic double layer[2] and can be significantly larger than the size of the core observed by TEM. In addition, one should remember than since the scattered intensity scales as D^6, larger particles tend to screen smaller ones. The results are given either in terms of intensity distribution, or of size distribution using the bimodal analysis algorithm provided by Malvern. Alternatively, $Z_{average}$ represents the diameter calculated from the cumulant analysis. Since viscosity is related to solvent composition and is an important parameter in DLS analysis, the vials were kept closed to limit change in solvent composition. The viscosity of the water:THF (80:20) mixture at 40°C (0.92 mPa.s) was taken from the work by Nayak.[3]

Electrocatalytic behaviour towards HER and OER.

The electrochemical responses were recorded using an Autolab electrochemical analyzer (PGSTAT 30 potentiostat/galvanostat from EcoChemie B.V.) in a three-electrode setup. A saturated calomel electrode (SCE) and platinum wire were used as the reference electrode and as the counter electrode, respectively. The potentials are reported against the reversible hydrogen electrode according to the following equation: E(RHE) = E(SCE) + 0.059 pH + 0.24. The working electrode is a polished glassy carbon disk electrode (GC) of 3 mm in diameter. Nanomarbles and nanocapsules were drop-casted from their aqueous suspensions onto the GC surface and the pristine clusters **1** and **2** were drop-casted from dichloromethane solutions. The amount of deposited material was quantified through QCM measurements. The variation of the QCM nominative frequency was converted to a mass according to the Sauerbrey equation: with k=1.1ngHz^{-1}. Typically, a 20 µL drop of nanocapsules solution gives 4.91 µg of nanocapsules. In all cases, the catalyst loading was adjusted to 0.35 mg/cm^2 in order to enable comparison. Electrochemical measurements were performed with a scan rate of 100 mV.s^{-1} using aqueous KNO_3 1 M (pH 7) as electrolyte, at an arbitrary catalyst loading of 0.35 mg/cm^2. The current was normalized against the geometrical area. The potentials were not corrected from the iR-drop.

Single-Crystal X-ray Diffraction.

Single crystals of $H_2[Mo_6Br^i_8(OH)^a_6].12H_2O$ were obtained from $Cs_2[Mo_6Br^i_8Br^a_6]$. The crystal structure measurements were carried out on APEX II Bruker AXS spectrometer using Mo-K_α X-ray wavelength (CDIFX, ISCR, Rennes). The structures were solved by direct methods using SIR97 program[4] and then refined with full-matrix least-square methods based on F^2 (SHELXL-2014)[5] through the aid of the WinGX platform.[6] Multi-scan absorption correction was applied using SADABS [G. M. Sheldrick, SADABS version 2014/5, SADABS Bruker AXS Inc., Madison, Wisconsin, USA.]. All non-hydrogen atoms were refined with anisotropic atomic displacement parameters. Hydrogen atoms were not considered in the structural model. Publishing data were computed using CRYSCALC program (T. Roisnel, local program, www.cdifx.univ-rennes1.fr/cryscalc).

Crystal data: crystal size = 0.16 × 0.08 × 0.07 mm^3, space group $R\ \bar{3}m$, T = 150(2)K, a = 15.2675(4) Å, c = 11.1594(3) Å, V = 2252.7(2) Å^3, Z = 3, empirical formula: $Br_8H_{32}Mo_6O_{18}$, M_f = 1535.17 g.mol^{-1}, ρ_{calc} = 3.395 g.cm^{-3}, θ range for data collection: 3.582 - 45.260°, 18107 reflections collected, 2244 unique reflections, R_{int} = 0.0484, completeness to theta max = 0.997, 32 refined parameters, Goodness-of-fit = 1.056, final R_1 [I > 2σ] = 0.0285, final wR_2 [I > 2σ] = 0.0550, largest difference peak and hole: +1.207 and -1.056 e.Å^{-3}.

Theoretical Calculations.

Quantum chemical calculations have been performed with the Gaussian 09 package.[7] The PBE exchange-correlation functional[8] has been used for all calculations in combination with the Def2TZVP basis set of Weigend and co-workers.[9,10] An ultrafine integration grid was used for all calculations (energy, geometry optimization and frequency) and tight convergence criteria were used for geometry optimizations. For geometry optimization and frequency calculation, O_h symmetry was used for $[Mo_6Br^i_8Br^a_6]^{2-}$ and $[Mo_6Br^i_8(NCS)^a_6]^{2-}$ motifs while no symmetry constraint was applied for other motifs.

2. Selection of the cluster species

The $[Mo_6X^i_8L^a_6]^{2-}$ cluster units crystallize with counter cations A^+ to form $A_2[Mo_6X^i_8L^a_6]$ solid state compounds (A = Cs^+, NH_4^+, $((C_4H_9)_4N^+)$; X^i = Cl, Br and I; L^a = halogen, $OOCC_nF_{2n+1}$, CN, NCS,…). On the chemical point of view, the natures of X^i and L^a drive the chemical stability of the whole $[Mo_6X^i_8La_6]^{2-}$ cluster unit. For instance, the oxidation potential of $[Mo_6X^i_8L^a_6]^{2-}$ decreases from 1.181, 0.969 and 0.525 V in acetonitrile (vs. the ferrocenium/ferrocene) for X^i = L^a = Cl, Br and I respectively.[11] Iodides oxidize irreversibly. Chlorides are more sensitive to exchange of inner ligands than iodides and bromides.[12,13] Therefore we decided to select X^i =Br which yield the most stable cluster core. Importantly, the stability in water and the possibility of exchange of apical ligands by OH^- or H_2O depend on the nature of L^a. On the other hand, the solubility depends on the nature of A^+. For instance, $((C_4H_9)_4N)_2[Mo_6X^i_8L^a_6]$ is fully insoluble in water and alcohol but is soluble in acetone, acetonitrile and THF. $Cs_2[Mo_6X^i_8L^a_6]$ (X^i = L^a = Cl, Br and I) is soluble in water but rapidly precipitates as aqua hydroxo compounds[14]. Such formation of aqua hydroxo complexes can be avoided when lowering the pH to 2 or when a 50/50 water/ethanol mixture is used instead of pure water. The substitution of Cs^+ by NH_4^+ leads to $(NH_4)_2[Mo_6X^i_8L^a_6]$ which is more stable in water for pH > 2 than $Cs_2[Mo_6X^i_8L^a_6]$. The stability is increased by the supplementary substitution of apical halogen by SCN groups that is linked to the cluster by a Mo-N bond.

Taking into account that the Ouzo method requested to start from a solution of cluster in THF, we selected the two bromide compounds **1** = $Cs_2[Mo_6Br^i_8Br^a_6]$ and **2** = $(NH_4)_2[Mo_6Br^i_8(NCS)^a_6]$ which show a solubility in THF above 1 mM. The compound, $(NH_4)_2[Mo_6Br^i_8Br^a_6]$ was excluded because its solubility in THF is lower than 1 mM.

3. Selected area electron diffraction (SAED)

The SAED show only diffuse rings, attesting the amorphous nature of the nanomarbles and nanocapsules.

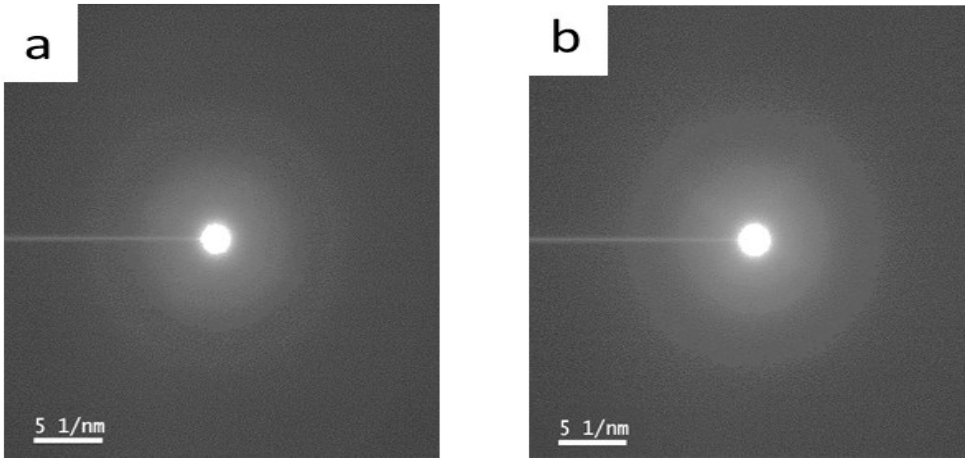

Figure SI-1: SAED of (a) nanomarbles obtained from 1 and of (b) nanocapsules obtained from 2.

4. Single-crystal X-Ray diffraction of $(H)_2[Mo_6Br^i_8(OH)^a_6].12H_2O$

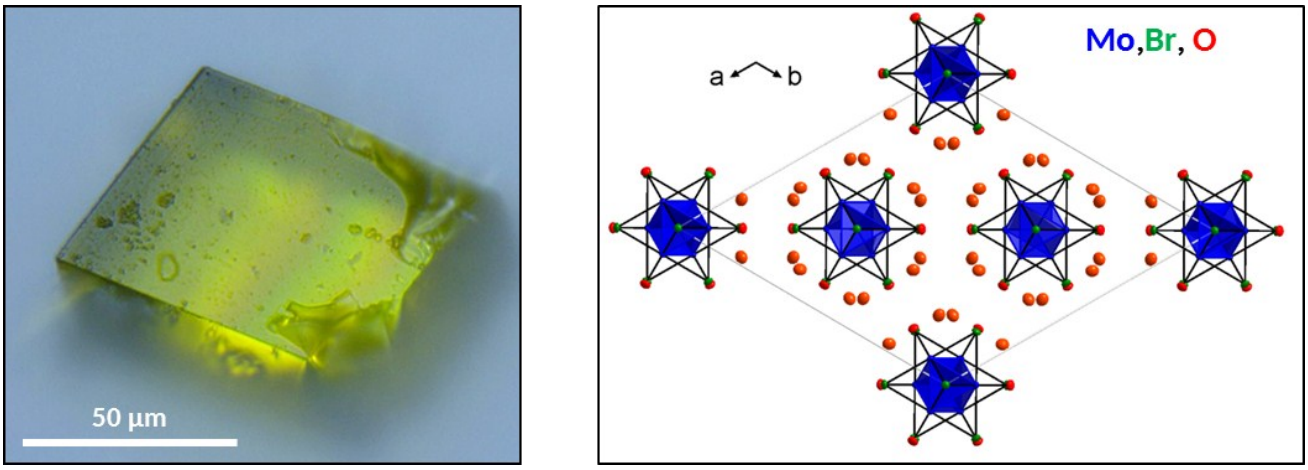

Figure SI- 2: (Left) Optical microscopy of $H_2[Mo_6Br^i_8(OH)^a_6].12H_2O$ crystal obtained by hydrolysis of 1; (right) Projection along the *c*-axis of the crystal structure of $H_2[Mo_6Br^i_8(OH)^a_6].12H_2O$ (Hydrogen atoms are not represented).

Table SI-1: Atomic coordinates, site occupancy and equivalent isotropic displacement parameters at T = 150 K of $H_2[Mo_6Br^i_8(OH)^a_6].12H_2O$

Atom	Site	x	y	z	Occ.	U(eq)
Mo	18h	0.1147(1)	x/2	0.5965(1)	1.00	0.0059(1)
$Br^i(1)$	6c	0	0	0.7877(1)	1.00	0.0090(1)
$Br^i(2)$	18h	0.2292(1)	x/2	0.4064(1)	1.00	0.0100(1)
O^a	18h	0.2423(2)	x/2	0.7103(2)	1.00	0.0147(4)
O (water)	36i	0.2106(2)	-0.0264(2)	0.8799(2)	1.00	0.0231(3)

Table SI-2: Average bond distances in $[Mo_6Br^i_8(OH)^a_6]^{2-}$ cluster units at 150K

Mo-Mo (Å)	Mo-Br^i (Å)	Mo-O^a (Å)
2.631(1)	2.618(1)	2.111(2)

5. Raman spectroscopy

Table SI- 3: Experimental and calculated Raman vibrations of cluster 1 and assignments. Calculated Raman vibrations are obtained on an isolated $[Mo_6Br^i_8Br^a_6]^{2-}$ motif of Oh symmetry while experimental vibrations are obtained on $Cs_2[Mo_6\ Br^i_8Br^a_6]$. [(a)] vibrational mode for which the group frequency concept does not apply.

Exp (cm^{-1})	Calculated (cm^{-1})	Calculated Intensity	Assignment
-	55	weak	Mo-Br^a bending T_{2g}
121	109	Moderate	Mo/Br^i/Br^a stretching E_g [(a)]
129	118	very weak	Mo-Br^i bending T_{2g}
132	135	very weak	Mo/Br^i/Br^a bending E_g [(a)]
145/149	143	Moderate	Symmetric Mo-Br^a stretching A_{1g}
174/178	159	weak	Asymmetric Mo-Br^i stretching T_{2g}
210	194	strong	Symmetric Mo-Br^i stretching A_{1g}
256	244	weak	Asymmetric Mo-Br^a stretching E_g
-	300	very weak	Asymmetric Mo-Mo stretching T_{2g}
322	316	weak	Symmetric Mo-Mo stretching A_{1g}

The analysis of the Raman spectrum of $(TBA)_2[Mo_6Br_8Br_6]$ was previously conducted by Schoonover and co-worker based on experimental and symmetry considerations and can be directly compared to the present work on $Cs_2[Mo_6Br_8Br_6]$.[15] The $[Mo_6Br^i_8Br^a_6]^{2-}$ cluster units belong to the O_h point group and display ten Raman active modes: $3A_{1g} + 3E_g + 4T_{2g}$. In their study, Schoonover et al. attributed with certainty the three A_{1g} modes corresponding to breathing motions of the Mo_6 cage, Br^i_8 face-bridging cube and apical Br^a_6 ligands.[15,16] However, less information was provided on the other modes. With the help of quantum chemical calculations, we herein provide attributions for the whole vibrational modes of the pristine cluster compound. The experimental values are reported Table SI-3 along with the theoretical values obtained at the density functional theory level, the symmetry and the assignment of each mode. Overall, the calculated frequencies are in good agreement with the experimental values with differences of ~10-20 cm^{-1}. Of course, the experimental frequencies are influenced by the chemical environment of the cluster unit in $Cs_2[Mo_6Br_{14}]$, so a perfect match is not expected. In terms of assignment, the correct symmetries are obtained with 3 A_{1g}, 3 E_g and 4 T_{2g} vibrational modes. The attribution of the A_{1g} modes is identical to the one proposed by Schoonover et al. The lowest frequency mode of T_{2g} symmetry is not observed experimentally due to the considered frequency range. However, among the three other modes, two corresponds to Mo-Br^i modes and one to Mo-Mo as given by the selection rules. For the Eg modes, the attribution is more complex. Indeed, the structure of $[Mo_6Br^i_8Br^a_6]^{2-}$ leads to symmetry coordinates that are significantly mixed in forming the normal modes and so the group-frequency concept breaks here. This point was already discussed by Schoonover et al. Consequently, the modes calculated at 109 and 135 cm^{-1} cannot be assigned to a particular group frequency. The symmetric Mo-Mo stretching of A_{1g} symmetry display a rather weak intensity as already observed by Schoonover et al. but is clearly present. However, the asymmetric Mo-Mo stretching of T_{2g} symmetry calculated at 300 cm^{-1} is not observed experimentally, neither by us or Schoonover, due to a very weak intensity. Note that the

two signals at 149 cm^{-1} (stretching A_{1g}) and 256 cm^{-1} (stretching E_g) are not observed in the aquahydroxo complex $H_2[Mo_6Br^i_8(OH)^a_6].12H_2O$ which supports their assignment to a Mo-Br^a modes. The same can be said for the signal at 121 cm^{-1} which demonstrates that, although it can hardly be assigned to a specific group, the contribution of Br^a is significant in this mode.

To understand the Raman spectra of the aquahydroxo complex $H_2[Mo_6Br^i_8(OH)^a_6].12H_2O$, we also performed calculations on an isolated $[Mo_6Br^i_8(OH)^a_6]^{2-}$ species. In that case, the presence of the hydroxyl groups breaks the O_h point group symmetry. Calculations were thus performed without symmetry. This significantly complicates the analysis of the results as all vibrational modes become Raman actives, even though most of them display a very weak intensity. Furthermore, strong mixing between the modes occurs which makes an analysis in terms of group frequency hardly possible. Nevertheless, three key results are obtained. First, an intense signal is calculated at 272 cm^{-1} which corresponds to the symmetric Mo-Mo stretching and 6 weak signal ranging from 298 to 283 cm^{-1} correspond to asymmetric Mo-Mo stretching. Those signals correspond to the large band experimentally observed between 275 and 300 cm^{-1}. Second, the symmetric Mo-O stretching is calculated at 520 cm^{-1} and 5 signals ranging from 490 to 486 cm^{-1} correspond to asymmetric Mo-O stretching. Those bands are unambiguously observed experimentally which confirm the hydrolysis of the $[Mo_6Br^i_8Br^a_6]^{2-}$ during the synthesis of the nanomarbles. Finally, 6 signals are calculated in between 724-715 cm^{-1} corresponding to Mo-O-H bending. Among them, the most intense one correspond to the symmetric mode at 722 cm^{-1}. This signal is not observed experimentally and the two bands at 875 and 925 cm^{-1} in $H_2[Mo_6Br^i_8(OH)^a_6].12H_2O$ remain unassigned. However, considering a $[Mo_6Br^i_8(OH)^a_6]^{2-}$ dimer bounded through two Mo-OH---OH-Mo motif (Figure SI-3), two signals appear at 890 and 898 cm^{-1}. Signals in this frequency range are thus indicative of the hydrogen bonding between the cluster units.

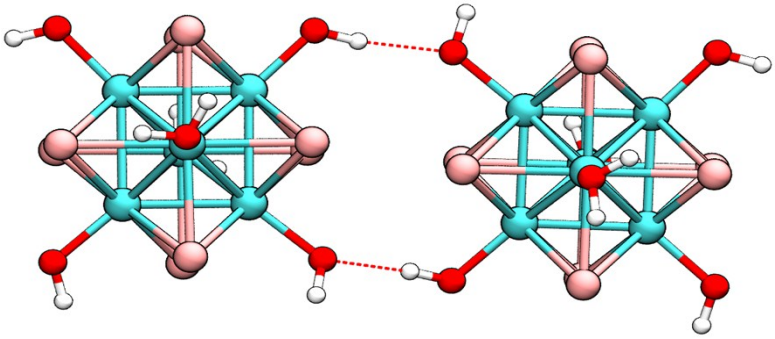

Figure SI-3: Neutral (each cluster is doubly protonated) structural model of a $[Mo_6Br^i_8(OH)^a_6]^{2-}$ dimer used to probe the influence of bonding between cluster units on their vibrational modes. Mo, Br, O and H atoms are represented by blue, pink, red and white spheres, respectively.

Table SI-4 Experimental and calculated Raman vibrations of precursor 2 and assignments. Calculated Raman vibrations are obtained on an isolated $[Mo_6Br^i_8(NCS)^a_6]^{2-}$ motif of Oh symmetry while experimental vibrations are obtained on $(NH_4)_2[Mo_6Br^i_8(NCS)^a_6]$. [(a)] vibrational mode for which the group frequency concept does not apply.

Exp (cm^{-1})	Calculated (cm^{-1})	Calculated Intensity	Assignment
118	109	weak	Mo-Br^i bending T_{2g}
124	119	weak	Asymmetric Mo/Br^i/NCS stretching E_g [(a)]
134	145	weak	Asymmetric Mo/Br^i/NCS stretching E_g [(a)]
178/183	173	strong	Asymmetric Br^i/NCS T_{2g} [(a)]
	184	weak	Symmetric Mo/Br^i/NCS stretching A_{1g} [(a)]
210	194	Very strong	Symmetric Mo/Br^i/NCS stretching A_{1g} [(a)]
301	292	Very strong	Asymmetric Mo-NCS stretching E_g [(a)]
323	307	Weak	Asymmetric Mo-Mo stretching T_{2g}
353	339	Very strong	Symmetric Mo-Mo stretching A_{1g} (*)
470/490	466	Weak	Bending S-C-N T_{2g}
829/839/849	881	Very strong	Asymmetric S-CN stretching E_g
	882	Very strong	Symmetric S-CN stretching A_{1g}
950	- NA -	- NA -	- NA -

If we now consider $(NH_4)_2[Mo_6Br^i_8(NCS)^a_6]$ (2) (table SI-4), above 2000 cm^{-1}, two signal calculated at 2080 (A_{1g}) and 2059 (E_g) cm^{-1} correspond to the symmetric and asymmetric CN stretching, respectively. The two signals centered at ~330 and 480 cm^{-1} can be assigned to S-CN stretching and S-C-N bending, respectively. They are thus fingerprint of the presence of the SCN species. The signal experimentally observed at 353 cm^{-1} can be mainly attributed to the symmetric Mo-Mo stretching. However, in contrast to $[Mo_6Br^i_8(Br)^a_6]^{2-}$ and $[Mo_6Br^i_8(OH)^a_6]^{2-}$ a significant contribution comes from the apical ligand, it thus also displays a symmetric Mo-NCS stretching character. The same is observed for the signal at 301 cm^{-1} which is mainly a Mo-NCS stretching mode but with a significant Mo-Mo stretching character. The group-frequency concept thus hardly applies to those two modes (353 and 301 cm^{-1}) which characterize both Mo-Mo and Mo-NCS stretching. However, they are related to the existence of the Mo-N bond. In between, at 323 cm^{-1}, the symmetric Mo-Mo stretching mode is observed with a much weaker intensity. The three following modes are more complex to interpret. They are calculated at 194, 184 and 173 cm^{-1} and should correspond to three experimental modes at 210, 183 and 173, the latter ones strongly overlapping. Those modes are strongly mixed and cannot be attributed to specific modes as they both contain some amount of: Mo-NCS, Mo-Mo and Mo-Br^i stretching for the signals at 194 and 184 cm^{-1} as well as Mo-N-C bending in the signal calculated at 173 cm^{-1}. This strongly contrasts with $[Mo_6Br^i_8(Br)^a_6]^{2-}$ and $[Mo_6Br^i_8(OH)^a_6]^{2-}$ where two Mo-Br^i stretching modes (symmetric and asymmetric) can be unambiguously attributed. The two next modes are also mixed with contributions from both NCS and Br^i while the last mode observed experimentally appears to be a bending Mo-Br^i vibration.

In the nanocapsules, if compared to the spectrum of $(NH_4)_2[Mo_6Br^i_8(NCS)^a_6]$, only minor changes are observed below 250 cm^{-1} which suggests that the $[Mo_6Br^i_8(NCS)^a_6]^{2-}$ cluster unit is preserved. In contrast to $[Mo_6Br^i_8(Br)^a_6]^{2-}$, no band disappear. However, the strong decay and broadening of the bands over 250 cm^{-1} is a striking feature of the Raman spectra of the nanocapsules. Nevertheless, most all the bands present in $(NH_4)_2[Mo_6Br^i_8(NCS)^a_6]$ are still present in the nanocapsule spectrum, although they are subject to frequency shifts. This seems to be in line with the presence of $[Mo_6Br^i_8(NCS)^a_6]^{2-}$ motifs but probably with a somewhat different chemical environment.

6. Luminescence measurements

Cluster compounds emission in the conditions of nanomarbles and nanocapsules synthesis.

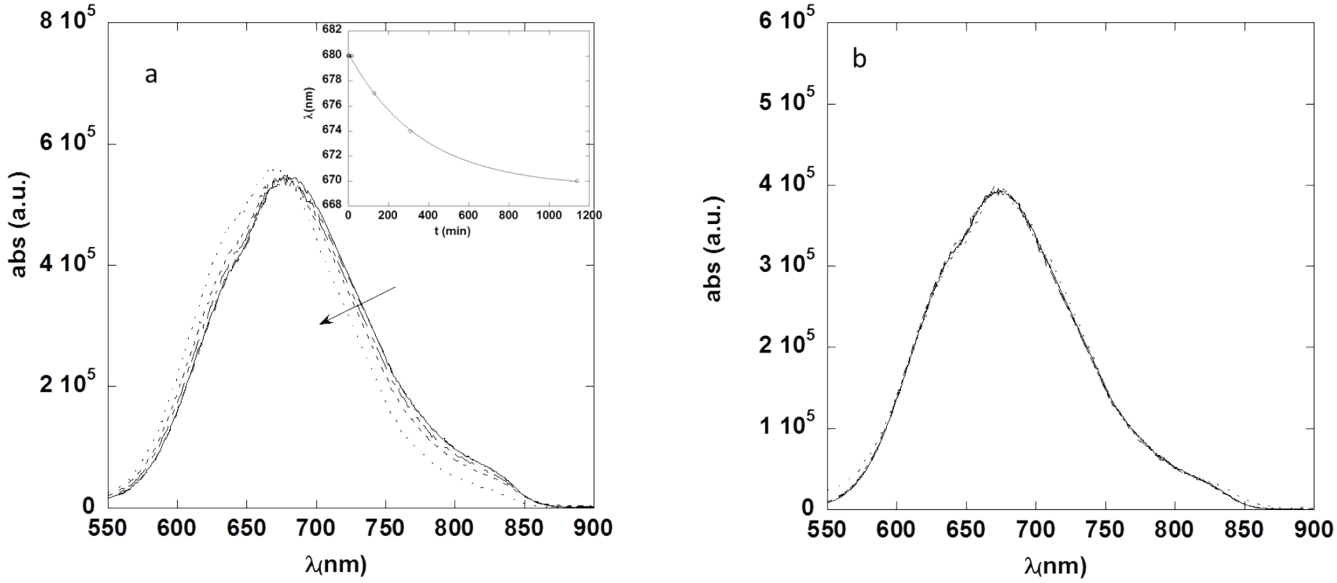

Figure SI-4: Time evolution of the emission spectra of cluster units water:THF solution (80:20): (a) cluster 1 at 0; 130; 310 and 1140 minutes; and (b) cluster 2 at 0; 10; 120 and 1440 minutes. λ_{exc} = 375 nm. Insert: time evolution of the emission maximum and fit with an exponential decay law.

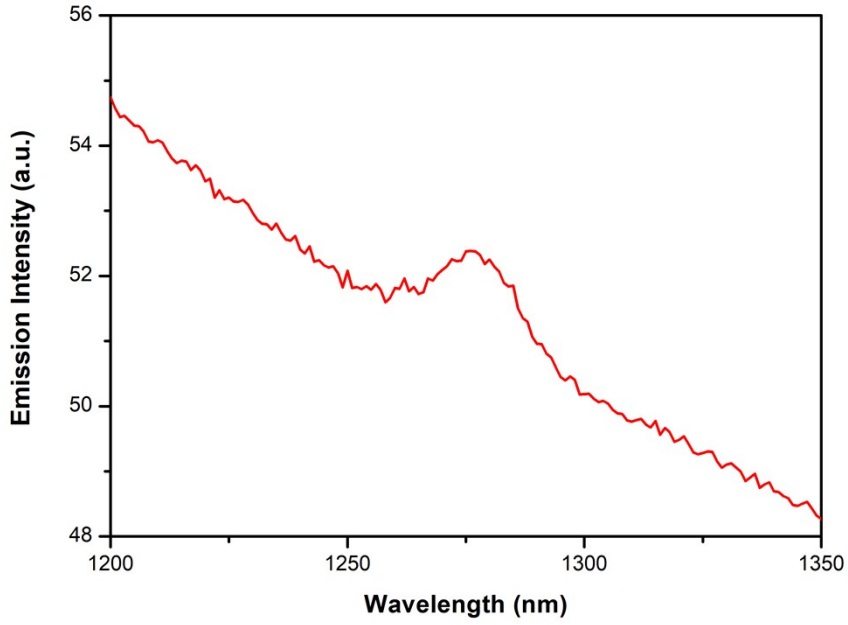

Figure SI- 5: Emission of singlet oxygen (O_2 ($^1\Delta g$)) from a powder of nanocapsules exposed to air. The production of O2 ($1\Delta g$) is photosensitized by the cluster. λ_{exc} = 375nm.

7. Formation of the nanomarbles and nanocapsules

The size distribution of nanomarbles and nanocapusles after 15h at 40°C in open vials was measured by Nanoparticle Tracking Analysis (NTA, Malvern Instrument) (Figure SI-6). For nanomarbles, it shows a main mode at a hydrodynamic diameter D_h=63nm, with a PDI=0.083 which indicates a narrow size distribution (mean diameter: 84.4nm, SD=24.3nm) as already observed by TEM. In contrast nanocapsules have a broad size distribution (mean diameter: 200 nm, SD = 71.7 nm).

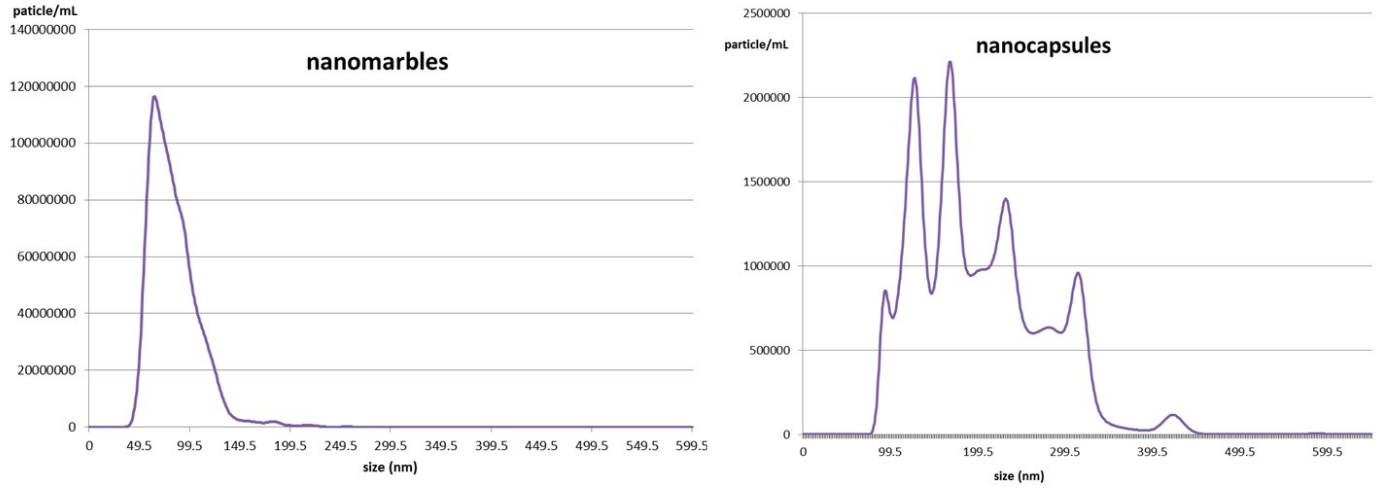

Figure SI- 6: Size distribution (hydrodynamic diameter) of the nanomarbles and nanocapsules after 15h at 40°C in open vials.

The mechanism of formation of the nanomarbles can be simply understood in terms of nanoprecipitation. Indeed, when water is added, the hydrolysis of the apical Br ligand yields an insoluble hydroxylated species which precipitates as dense nanoparticles of uniform size, as it is generally the case in diluted nanoprecipitation systems.

The mechanism of formation of the nanocapsules obtained from **2** was monitored by TEM and DLS over time (Figure SI-7). Right after adjusting the solvent composition to water:THF (80:20), the closed vials were set at 40°C. The TEM observations achieved a few minutes after mixing all components (t=0) show vesicles with relatively heterogeneous sizes ranging from 20 to 80 nm. The DLS measurements at the same stage confirm the presence of large particles (D_h ~ 200 nm) that dominates in the scattered intensity (Figure SI-7a). However, analysis by numbers reveals that the largest population consists of scatterers with a size D_h ~ 2 nm, corresponding to cluster units. These findings indicate the coexistence of free and surface-adsorbed cluster units at the first stage of the process. After this initial stage, the scattering signal associated with the free cluster units becomes rapidly undetectable. Interestingly, between 5 and 10 h, TEM observations show that the size of the nanocapsules decreases from D = 52 ± 17 nm to 35 ± 6 nm with a narrower size distribution. This is a unique case of spontaneous size narrowing of capsules, and is at present not understood. However, it can only be allowed by the dynamical exchange of cluster species. After 10 hours, the capsule shell is still very thin and shows wrinkles when dried on TEM grids. Then, the thickness of the shell increases significantly to over 20 nm at 58 h (Figure SI-8), which is also observed after several weeks at room temperature (Figure SI-9). At t = 24 h and later a few capsules sizing over several hundreds of 100 nm are observed (Figure SI-10). Interestingly, it does not occur when samples are kept at room temperature and most probably results from the building of internal pressure within the capsules. We propose the following mechanism for the formation of the nanocapsules. In water : THF mixtures, the cluster units 2 rapidly adsorb at liquid/liquid interfaces, which stabilizes solvent droplets formed by Ouzo effect. Dissolved clusters and dense aggregates are also present and feed the thickening of the shell. Indeed, a close observation of the TEM grids also revealed the presence of aggregates at 5 and 10 h (Figure SI-11), which were not observed later.

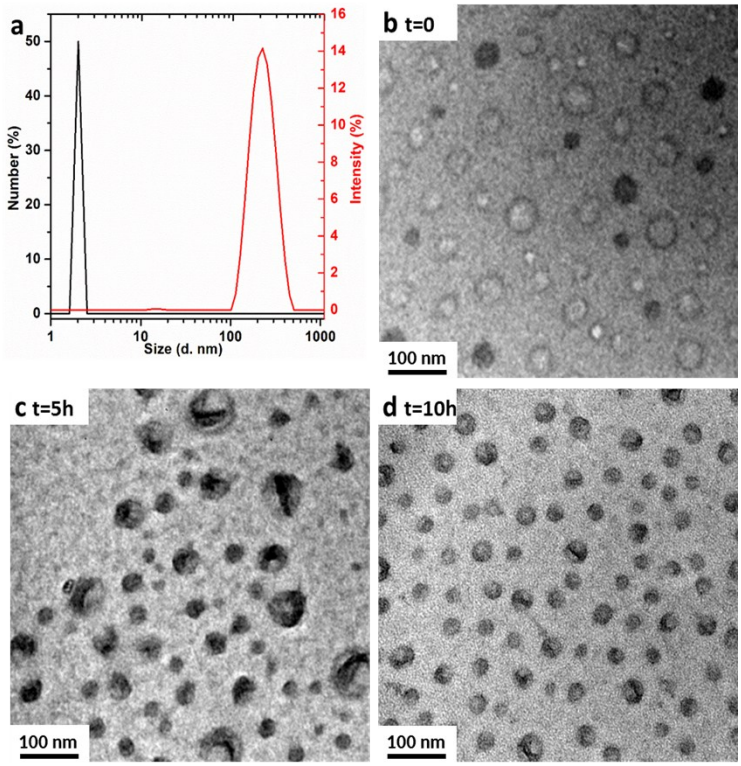

Figure SI- 7: Time evolution over 10 hours of nanocapsules obtained from 2 at 40°C in closed reactor. (a) DLS measurements of 2 in water:THF mixture at the initial stage; (b-d) TEM micrographs of the suspension at t=0; 5 h and 10 h.

The thickening of the capsule wall was clearly observed for t>10h when the samples were heated at 40°C. Measurements were achieved from TEM images (Figure SI-8), with typically 50 measurements over 15 different capsules. The thickness was arbitrarily set to 0 for t<10 h and estimated at ca 3 for t=10 h. Capsules with the same thickness are also obtained without heating, after 100 days (Figure SI-9).

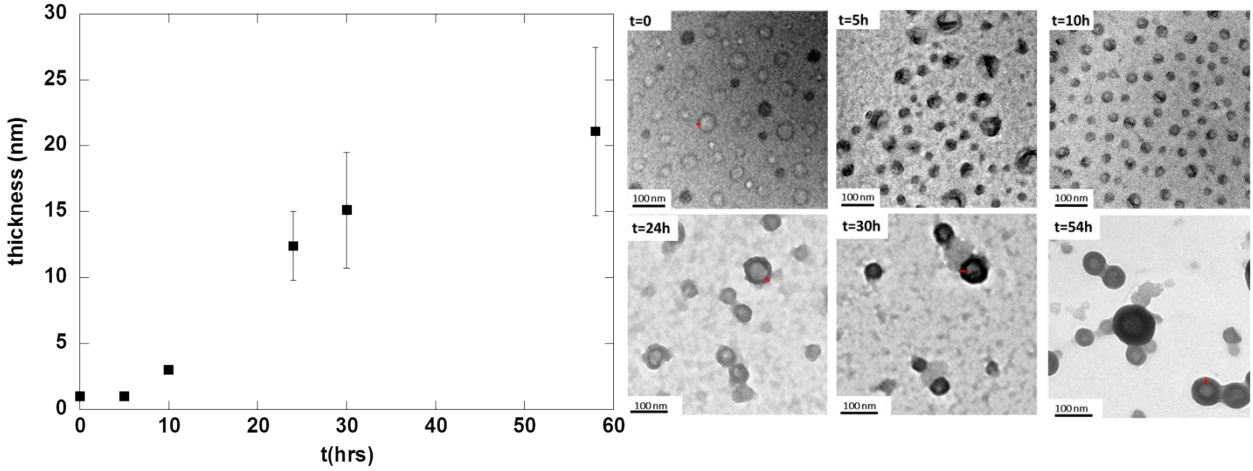

Figure SI- 8: Time evolution of the thickness of the wall of capsules obtained from cluster 2 at 40°C in closed reactor, and corresponding TEM snapshots at t=0; 5; 10; 24h; 30h; and 54h.

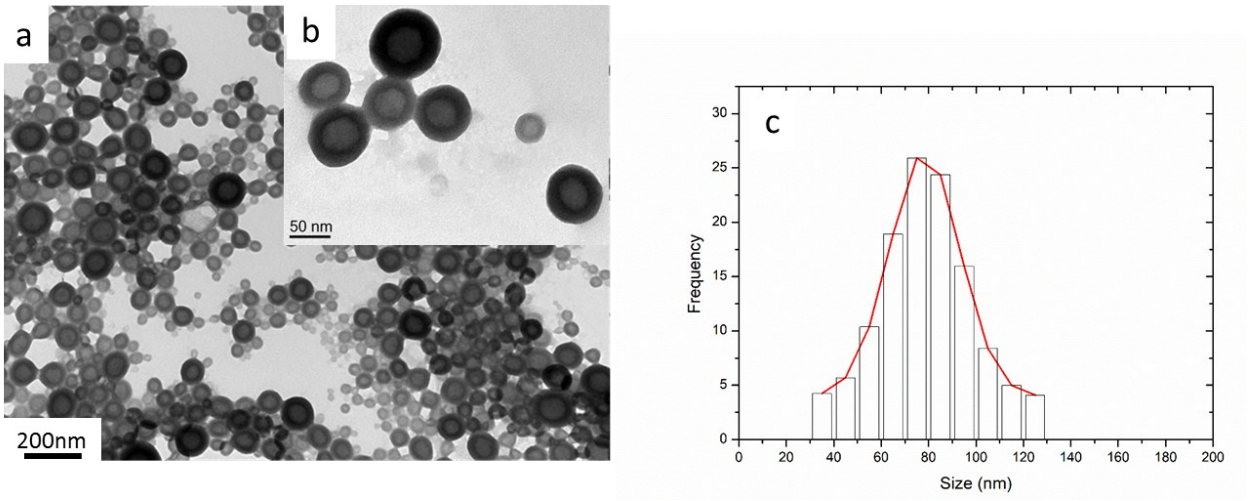

Fig SI-9: (a-b) TEM of nanocapsules formed at room temperature after 100 days and (c) size histogram of the diameter of the capsules.

Beyond 10 hours, large capsules (100nm) appear in the suspension, in very low number, and induce a burst in the scattering signal measured by DLS ($Z_{average}$, Figure SI-10). This is not observed when samples were kept at room temperature. Interestingly, the wall of the large capsules is not thinner than that of small capsules, indicating that they are not formed by swelling from the smaller ones. Therefore, we hypothesize that the large capsules form de novo from free cluster units.

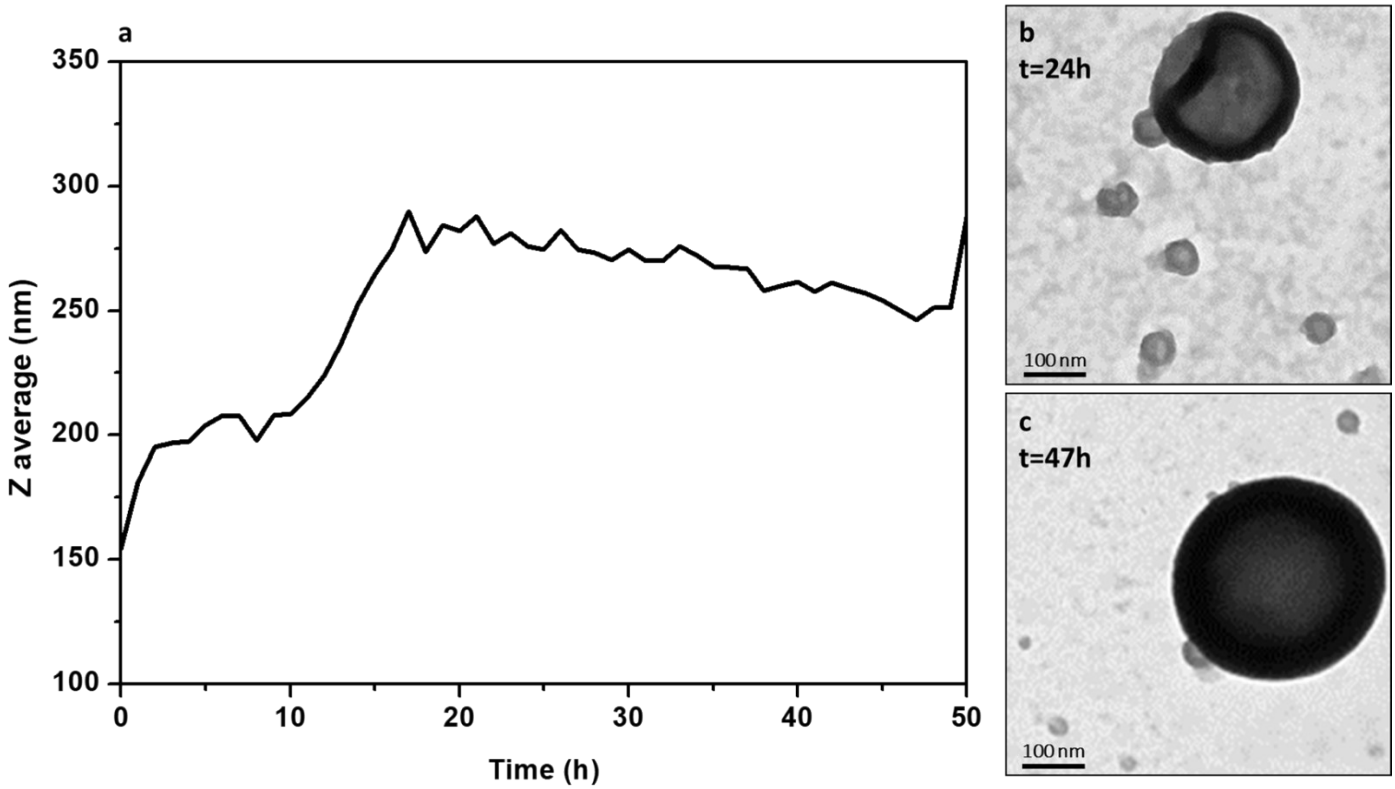

Figure SI- 10 (larger capsules): (a) Time evolution of the Z_{ave} in suspensions of 2 in water:THF mixtures at 40°C in closed reactor. TEM snapshots at (b) t=24 h; (c) t=47 h of large capsules.

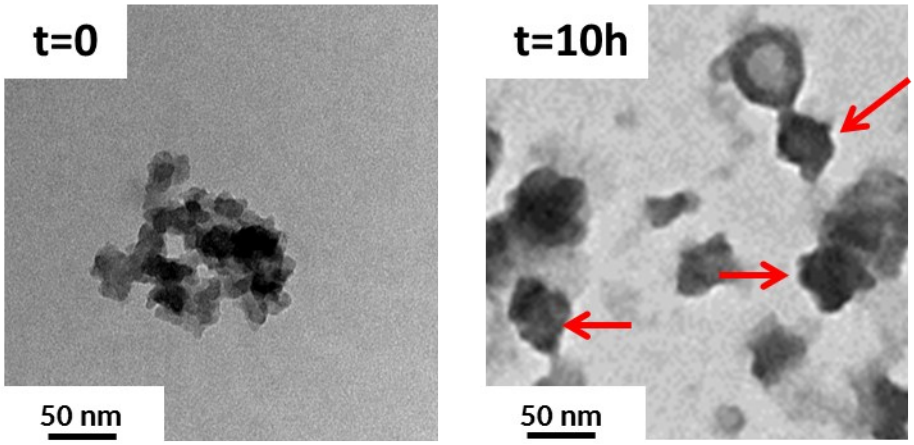

Figure SI- 11: TEM showing aggregates of cluster units in suspensions of 2 in water:THF mixtures at 40°C in closed reactor at t=0 and t=10 h.

8. Comparison of HER performance in neutral or close-to-neutral media with some molecular electrocatalysts

Table SI-5. Comparison of HER performance in neutral or close-to-neutral media with molecular catalysts

Molecular catalyst	**Exptal. conditions**	**Catalyst loading**	**Onset over-poten-tial (mV)[1]**	**Current density (mA. cm^{-2})**	**Overpotential (mV) at corresponding current density**	**ref**
CoP_4N_2	Neutral buffer Solution Mercury pool electrode	1 mM	80	10	430	Energy. Environ. Sci. 2017, 7, 329
Ni(cyclam)$^{2+}$ and Ni_2(biscyclam)4+	pH 7-8 buffer solution mercury pool electrode	0.2 mM 0.1 mM	560 400	nd	nd	Inorg. Chem. 1988,27, 1986
$Co(PY_5Me_2)$ PY = 2,6bis(1,1-bis(2-pyridyl)ethyl)pyri-dine	Neutral buffer solution Mercury pool electrode	38 µM	240	nd	nd	J. Am. Chem. Soc. 2011, 133, 9212
Acetylated cobalt microperoxidase-11	Neutral buffer solution Mercury pool	1 µM	600	CPE applied pot.[2]	900	J. Am. Chem. Soc. 2014, 136, 4
Co(II)tetrakis-(*p*-sulfonatophenyl)p orphyrin	Neutral buffer solution Adsorbed onto glassy carbon electrode	nd	409	CPE applied pot[2].	970	Chem. Commun. 2015, 51, 15067

Ni complex with amine-pyridine pentadentate ligands	Neutral buffer solution Mercury pool electrode	5 µM	>700 mV	nd	nd	Chem. Commun. 2014, 50, 14153
Fe complex with pentamethyldi-ethylenetriamine	Neutral KCl solution Deposited onto carbon electrode	nd	297	10	367	ACIE, 2015, 54, 14824
Co complex with tripyridine-diamine ligand	Neutral buffer solution Mercury pool electrode	5 µM	550	CPE applied pot [2]	650	Chem. Commun. 2013, 49, 9455
Copper(II)-L complex with H_2L=2,3-bis(2-hydroxybenzylideneimino)-2,3-butenedinitrile	Neutral buffer solution Carbon electrode	2.2 µM	320	CPE applied pot.[2]	817	Int. J; Hydrogen Energy, 2014, 39, 13972
Diironbenzenedithiolate complex	Neutral buffer solution but acid is added SDS micellar medium Mercury pool electrode	60 µM	nd	0.5	240	Energy Environ. Sci. 2012,5, 7757
Diiron-benzenedithiolate complex	Neutral buffer solution Catalyst immobilized in bilayer vesicles Screen-printed carbon electrode	n.d.	420	CPE applied pot. [2]	640	ChemElectro-Chem, 2018,5,20

[1] the overpotential is defined as the difference between the reversible potential of the couple H_2/H^+, i.e. -420 mV at pH 7, and the potential where electrocatalysis occurs. [2] benchmarking current density is not mentioned but constant potential electrolysis is run for producing an optimum amount of H_2.

[1] K. Kirakci, S. Cordier, C. Perrin, *Z. Für Anorg. Allg. Chem.* **2005**, *631*, 411–416.
[2] D. R. Grisham, V. Nanda, *Proteins Struct. Funct. Bioinforma.* **2018**, *86*, 515–523.
[3] J. N. Nayak, M. I. Aralaguppi, B. V. Kumar Naidu, T. M. Aminabhavi, *J. Chem. Eng. Data* **2004**, *49*, 468–474.
[4] A. Altomare, M. C. Burla, M. Camalli, G. L. Cascarano, C. Giacovazzo, A. Guagliardi, A. G. G. Moliterni, G. Polidori, R. Spagna, *J. Appl. Crystallogr.* **1999**, *32*, 115–119.
[5] G. M. Sheldrick, *Acta Crystallogr. Sect. C Struct. Chem.* **2015**, *71*, 3–8.
[6] L. J. Farrugia, *J. Appl. Crystallogr.* **2012**, *45*, 849–854.
[7] Frisch, M. J., Trucks, G., H. Schlegel, G. Scuseria, M. Robb, J. Cheeseman, G. Scalmani, V. Barone, G. Petersson, H. Nakatsuji, et al., *Gaussian 09*, Gaussian, Inc., Wallingford CT, **2016**.
[8] J. P. Perdew, K. Burke, M. Ernzerhof, *Phys. Rev. Lett.* **1996**, *77*, 3865–3868.
[9] F. Weigend, R. Ahlrichs, *Phys. Chem. Chem. Phys.* **2005**, *7*, 3297.
[10] F. Weigend, *Phys. Chem. Chem. Phys.* **2006**, *8*, 1057.
[11] K. Kirakci, P. Kubát, J. Langmaier, T. Polívka, M. Fuciman, K. Fejfarová, K. Lang, *Dalton Trans.* **2013**, *42*, 7224–7232.
[12] M. H. Chisholm, J. A. Heppert, J. C. Huffman, *Polyhedron* **1984**, *3*, 475–478.
[13] J. C. Sheldon, *J. Chem. Soc. Resumed* **1962**, 410–415.
[14] G. Daigre, J. Cuny, P. Lemoine, M. Amela-Cortes, S. Paofai, N. Audebrand, A. Le Gal La Salle, E. Quarez, O. Joubert, N. G. Naumov, et al., *Inorg. Chem.* **2018**, *57*, 9814–9825.
[15] J. R. Schoonover, T. C. Zietlow, D. L. Clark, J. A. Heppert, M. H. Chisholm, H. B. Gray, A. P. Sattelberger, W. H. Woodruff, *Inorg. Chem.* **1996**, *35*, 6606–6613.
[16] M. K. Simsek, D. Bublitz, W. Preetz, *Z. Für Anorg. Allg. Chem.* **1997**, *623*, 1885–1891.